City, University of London Institutional Repository

This is the accepted version of the paper.

This version of the publication may differ from the final published version.

Influence of self-adaptive hairy flaps on the stall delay of an airfoil in ramp-up motion

Christoph BRÜCKER, Christoph WEIDNER

Institute of Mechanics and Fluid Dynamics, TU Bergakademie Freiberg, 09599 Freiberg, Germany

Phone: +49 (0) 3731-39-3833. Corresponding author: bruecker@imfd.tu-freiberg.de

Abstract. It is known in the case of some birds that the coverts on the upper side of their wings pop-up under critical flight conditions such as the landing approach, thus acting like a brake on the spread of flow separation. Taking experimental investigations as its basis, this paper deals with the influence of various configurations of self-adaptable hairy flaplets located on the lower half of the wing and with chord-length c (dense rows of slender elastomeric flaps, L=0.05c, 0.1c, 0.2c) on the flow around an NACA0020 airfoil at low Reynolds number flow (Re=77×10^3). Flow evolution along the airfoil when in ramp-up motion (α_0=0, α_s=20°, reduced frequency k=0.12) was measured with and without hairy flaps, with growth in the chord-normal thickness of the separation region above the airfoil investigated in order to determine stall onset time Ts. Whereas small flaps with L=0.05c do not change the overall stall process, it was possible to use configurations with L=0.1c (double-row, triple-row configuration) to delay stall onset Ts by a factor of around 2-4 when compared with the clean airfoil. The motion of the flaps and the flow field were measured simultaneously at high temporal resolution using high-speed PIV. Correlation between flap motion and velocity distribution showed that backflow induced by vortex structures is indeed prevented by the hairy flaps. A significant difference was identified in the shear-layer roll-up process, which was almost regular and locked with the fundamental frequency on the covered airfoil with no signs of non-linear growth over longer periods. By way of contrast, in the case of the clean airfoil the early merging of the shear-layer vortices and a rapid increase in the thickness of the separation region were observed. It is

therefore concluded that mode locking is achieved between flap rows with an interspacing of 0.15c-0.2c, while the fundamental shear-layer roll-up wavelength measured ($\lambda_0\approx$0.15c-0.2c) indicates the relevance of flap row arrangement at the specific Reynolds number. Furthermore, interaction between shear-layer vortices and flaps in the row furthest downstream leads to the beneficial modification of the trailing edge flow in a way which increases bound circulation.

Key words: separation control, stall delay, hairy flaps, mode locking

1. Introduction

Flow over an airfoil tends at increasing angle of attack to separate on the suction side of the wing and causes therefore a dramatic decrease in aerodynamic lift (stall). A recent study into the mechanism of stall onset showed that it is promoted by the occurrence of non-linear disturbances in the shear layer formed in the boundary layer above the wing. The mechanism that results in the detachment of the dynamic stall vortex from the airfoil has been identified as vortex-induced separation caused by strong viscous interactions in the form of vortex pairing (Mulleners and Raffel, 2012, 2013). Birds have effective means of dealing with such critical flight conditions, with their feathers popping up if flow separation starts to develop on the upper side of their wing (Carruthers et al. 2007, also see Figure 1). These small, flexible coverts counteract backflow and prevent an abrupt breakdown in lift. This self-adjusting mechanism has been interpreted as a biological high-lift device assuming that a delay in flow separation results in higher lift at lower flight speeds (Liebe, 1979; Liebeck, 1978; Bramesfeld and Maughmer, 2002; Carruthers et al., 2007). Schatz et al. (2004) have shown that a self-activated spanwise flap near the trailing edge can enhance lift by more than 10% at a Reynolds number of $Re=1\text{-}2\times10^6$. Schlüter (2009) has demonstrated that lift-breakdown at low Reynolds numbers ($Re=30\text{-}40\times10^3$) and increasing angles of attack is less developed in the case of an airfoil with passive flaps than one without flaps. As a further test of this passive

separation control mechanism, Favier et al. (2009) conducted a numerical investigation into a cilia-like hairy coating attached to a two-dimensional circular cylinder at a Reynolds number of Re=200. Their results showed that such a coating is able to reduce overall drag by 15% and lift fluctuation by 44%. A similar result was also obtained at much higher Reynolds numbers in experiments involving a cylinder with flexible flaps similar to those used in the present study (Kunze and Brücker, 2012). A numerical study of the effect of hairy coatings on an NACA0012 airfoil was performed by Venkataraman and Bottaro (2012). They found coating parameters to decrease drag oscillations by approx. 11% and increase lift by approx. 9% under separated flow conditions at Reynolds number Re=1100 and angle of attack α=70°.

Figure 1. A falcon with popped-up feathers (left: frontal view, right: side view) during gliding flight before landing (from the measurement campaign documented in Ponitz et al. 2014).

Further studies have been carried out in order to substantiate the increase in lift achieved using other passive structures (Bechert et al., 1997). Hu et al. (2008) recently showed flexibility to be a key contributing factor to passive separation

control. In addition, even near-wall turbulence can be modified considerably using flexible structures (Brücker 2011).

A comparison of the action of fixed and free-moving effectors has been drawn up by Johnston and Gopalarathnam (2012). The fixed-deployment effectors represented a useful means of studying the influence on the flow field and airfoil surface pressures while maintaining control over the deployment angle. Both lift and drag are dramatically improved at angles of attack past the airfoil's normal stall angle, with improvements diminishing after an effector angle of 60°. At these angles of attack, the free-moving effector delivers drag and pitching moment curves that lie between the respective curves for fixed effectors at 30° and 45° angles. Johnston and Gopalarathnam used the method of oil flow visualization to confirm the separation delay caused by the effector at high angles of attack (i.e. higher than that at which the clean airfoil stalls). With the exception of the numerical studies drawn up by Schatz et al. 2004, however, there has to date been no detailed analysis of the fluid-structure interactions that might shed further light on the mechanism of stall delay. A number of more detailed studies have nevertheless recently been carried out in order to gain an improved understanding of the dynamics of stall onset (Mulleners and Raffel, 2012, 2013). A better appreciation of the processes involved in stall onset will pave the way for insights into the cause of stall delay.

The work described herein focusses on passive control using self-adaptive flexible structures. To this end, various hairy flap configurations were attached to the suction side of an NACA0020 airfoil and the flow during ramp-up motion investigated with the aid of experiments.

2. Experimental set-up

2.1. PREPARATION OF THE AIRFOIL

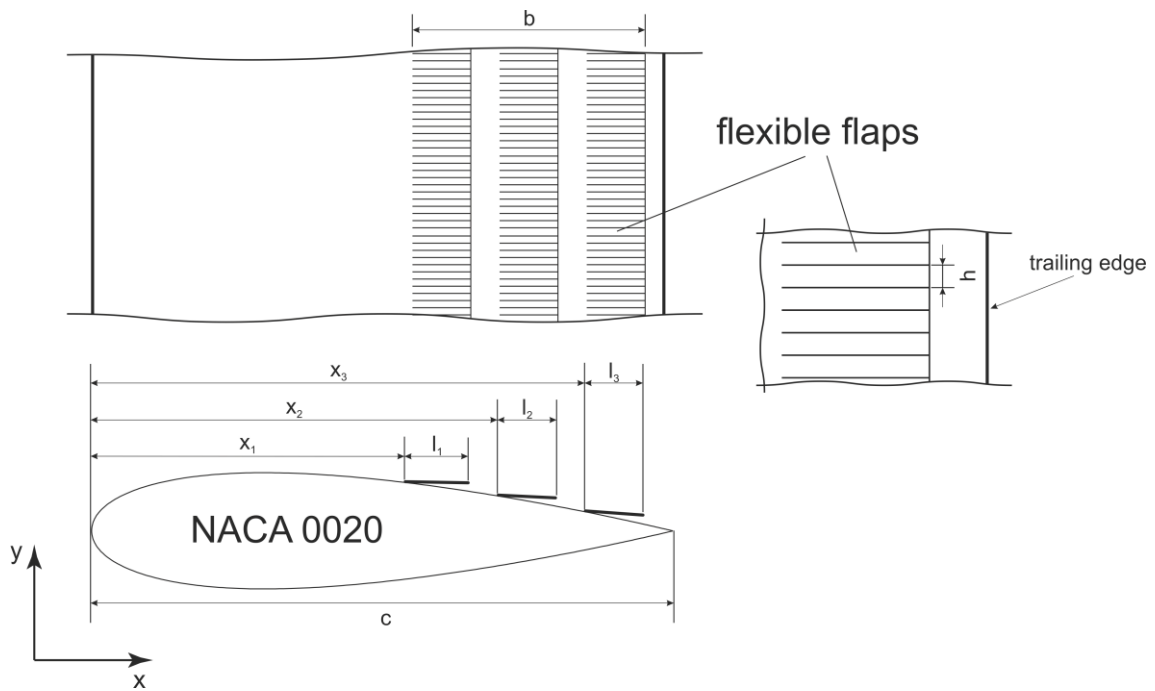*Figure 2:* Dimensions of the NACA0020 airfoil and parameters of the hairy flapconfiguration

A NACA0020 profile with a chord length of $c = 0.2$m and a spanwidth of 0.5m was selected for the experiments and tested in a uniform water flow. One half of

the airfoil's span was equipped with a thin rubber foil carrying an array of flexible flaplets made from an elastomer (Wacker RT 601 A and B). The two ingredients of the rubber were mixed, vacuumed and moulded to form thin foils (thickness b_F=2mm). Once the curing process was finished, the contours of the flexible hairy flaps were carved out of the foil. Finally, the foil with the flaps was attached to the airfoil. The flaps had a Young's modulus of E_F=1.7MPa and a density of ρ_F=1.2 kg/m^3. All flaps had a width of h_F=5mm (equal to interspacing) and were free to move in chord-normal direction (elevation direction). Flap length L_F was varied between 10, 20 and 40mm. Dimensionless bending stiffness K was defined as

$$K = EI / \rho L^3 U_\infty^2 = \frac{E\, h_F}{12} \left(\frac{b_F}{L_F} \right)^3 \frac{1}{\rho U_\infty^2}$$

and ranged between 4×10^{-2} (L_F=10mm) and 5×10^{-4} (L_F=40mm) for the various flap lengths. Overall, the structures bent easily in accordance with the flow and pressure forces acting upon them.

A typical flaplet arrangement is shown in Figure 1; the corresponding coordinates are given in Table 1.

No	π_{fill}	l_1	l_2	l_3	x_1	x_2	x_3	b	$T_S/T_{S_{ref}}$
	1/c								
ref	0	-	-	-	-	-	-	-	-
1	0.28	0.05	0.05	-	0.58	0.88	-	0.35	1
2	0.38	0.10	0.05	-	0.58	0.93	-	0.40	1.2
3	0.50	0.10	0.10	-	0.58	0.88	-	0.40	1.3
4	0.57	0.10	0.10	-	0.58	0.78	-	0.35	2

| 5 | 0.75 | 0.20 | 0.10 | - | 0.58 | 0.88 | - | 0.40 | 1.3 |
| 6 | 0.75 | 0.10 | 0.10 | 0.1 | 0.58 | 0.73 | 0.88 | 0.40 | 4.3 |

Table 1: Parameters of investigated flap configurations; reference case: NACA0020 airfoil without flaps; No.1 – No.6: hairy flap-configurations; non-dimensional fill factor $\pi_{\text{fill}} = ((l_1+l_2+l_3) / b)$; stall onset time Ts for the coated airfoil relative to Ts$_{\text{ref}}$ for the clean airfoil

Various arrangements were tested in order to investigate different numbers of flaplets in spanwise direction and their effect on efficient passive separation control. Earlier studies by Schatz et al. (2004) showed that the flaps are at their most active in the downstream half of the chord, thus preventing the growth of the separation region early in the stall process. The best effector configuration seems to be 10–30% of the chord length, with the leading edge of the effector positioned to the rear of the 0.5 x/c location and the trailing edge of the effector positioned at least 0.01 x/c in front of the trailing edge of the airfoil in order to properly respond to flow separation (Johnston & Gopalarathnam 2012). Only the chord-wise section of the lower half of the airfoil ($0.58 <= x/c <= 0.98$) was therefore covered with flaps. Non-dimension fill factor π_{fill} (see Table 1) was defined in order to determine the surface covered by the flaps relative to the selected chord section. The maximum fill factor was 75%, the minimum fill factor 28%. As it was not possible to create overlapping flaps, the selected chord segment could only be filled with a maximum of three rows at a flap length of L_F=0.1c (triple configuration). Smaller flaps with a length of $L_F = 0.05c$ were expected to be uneffective due to their insufficient reach into the separation

region, and were therefore only studied in two configurations. On the other hand, flaps with a length of $L_F = 0.2c$ (see experiment no. 5) exhibited complex bending behaviour as a result of their slenderness, and did not move in regular patterns normal to the surface but instead twisted with considerable bending in a spanwise direction due to their flexural instability and flutter. A clear correlation with the flow dynamics could not be drawn under such conditions. The most relevant configurations to the studies carried out were therefore those characterized by $L_F = 0.1c$ in single (approximated by no. 2), double (no. 3, 4) and triple configuration (no. 6). The latter represented the maximum number of rows that could be fitted in the predefined chord section.

The surface of the airfoil was coloured white and the trailing edges of the flaps painted in black in order to ensure that suitable records of the motion of the hairy flaps were created using the high-speed PIV measurements (see Figure 3).
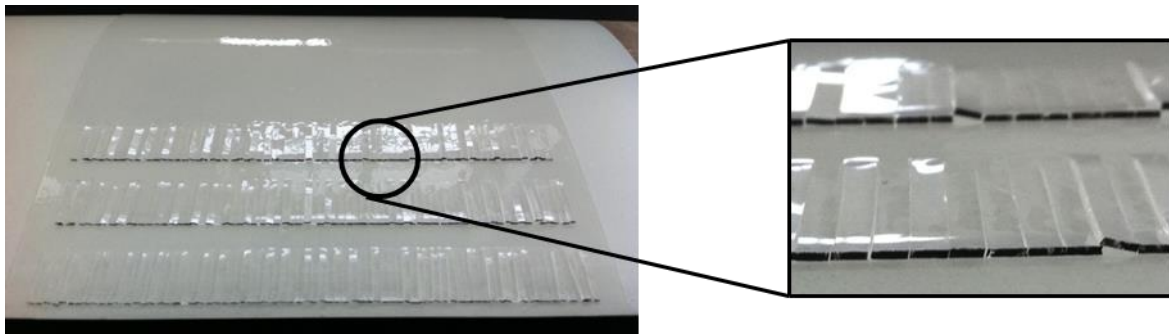

Figure 3: NACA0020 airfoil with flexible hairy flaps (No. 6).

A side view of the flaps when in action within the flow is shown in Figure 4 in

order to illustrate typical elevation during interaction with the flow when the airfoil is in pitched position (α=17.5°). Note the variation in deployment along the span, which is evident in the fuzzy structure where the flaplets are positioned. At rest the flaps lie flush with the surface.
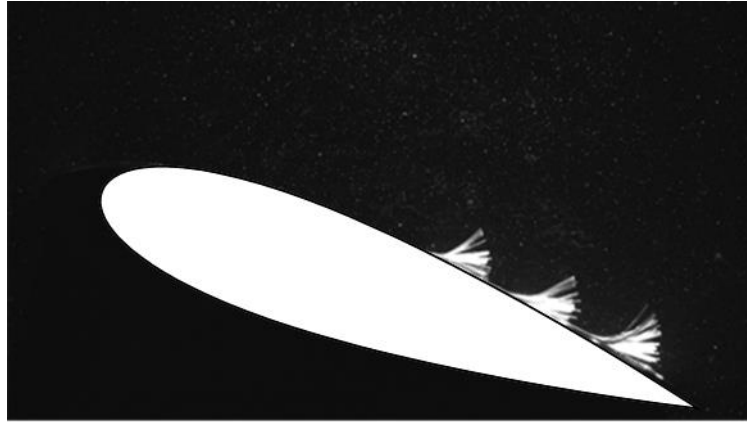

Figure 4: Image of the field of view for a hairy flap configuration (No. 6) at constant angle of attack α=17.5°.

2.2. EXPERIMENTAL METHODS

The influence of the flexible flaps on the flow around a NACA0020 airfoil with a Reynolds number of Re = 77×10^3 was investigated in a water channel at a bulk flow velocity of U_∞ = 0.38m/s. As the stall process is qualitatively similar in the case of airfoils subjected to either oscillating or ramp-type motions (McCroskey 1981), the latter motion type was chosen for reasons of better synchronization between measurement technique and airfoil motion. A diagram of the experimental setup is provided in Figure 5. The dimensions of the transparent test

section were 0.4m (width) × 0.4m (height) × 1.5m (length). The airfoil was mounted on the top of the water channel. Figure 4 shows an image recorded with a field of view of FOV=330×170mm^2. Measurements were first carried out at a constant angle of attack ($\alpha = 17.5°$) using standard 2D DPIV as a reference case. Ramp-up experiments were subsequently carried out. To this end, a linear traverse at the top of the water channel (see Figure 4) was used to turn the airfoil at a constant rate ($\partial\alpha / \partial t = \dot{\alpha} = 13,3° / s$) from zero angle of attack $\alpha_0 = 0$ to final state $\alpha_1 = 20°$, which represented the ramp-up amplitude (the rotation axis was located at x/c=0.275, y/c=0). Dimensionless representation is calculated with the aid of reduced frequency k (defined as $k = \pi\dot{\alpha}\cdot c / U_\infty$), which in the case of the experiments carried out amounted to $k = 0.12$ and was therefore similar to the state investigated in Mulleners & Raffel (2012). Standard DPIV recordings were taken with camera #1 (PCO 1600, 1600×1200px resolution, recording frequency 14Hz) and a pulsed Nd:YAG laser (Continuum Minilite). The DPIV vector fields were processed using Dynamic Studio V2.30 (Dantec Dynamics) with an adaptive cross-correlation algorithm on a 32×32px grid with an overlap of 75% and a peak validation algorithm. The velocity vectors were then locally smoothed using a moving average filter with a 5×5 kernel size.

A further round of experiments sawflap motion and flow field measured simultaneously at high temporal resolution (high-speed PIV). This involved the use of two high-speed cameras (Photron Fastcam RS, 1024×1024px resolution, recording frequency 500Hz). Camera #1 was used for high-speed PIV

recordings; Camera #2 pointed through a glass plate onto surface mirror 2 (positioned in the water channel downstream of the airfoil at a distance of 6*L*) and was synchronized with a flash lamp (see figure 5), which flashed in between the laser pulse pauses. This ensured that there was no cross-over between the PIV images and reflections from the flaps and vice versa. The light sheet was formed using a 10mJ Nd:YLF high-speed laser with double-lens optics and a mean wavelength of 527nm (Coherent Evolution). The dimension of the field of view used for the high-speed PIV measurements was $320{\times}320$mm^2. Flap tip positions were tracked in all images using image processing and edge detection algorithms.
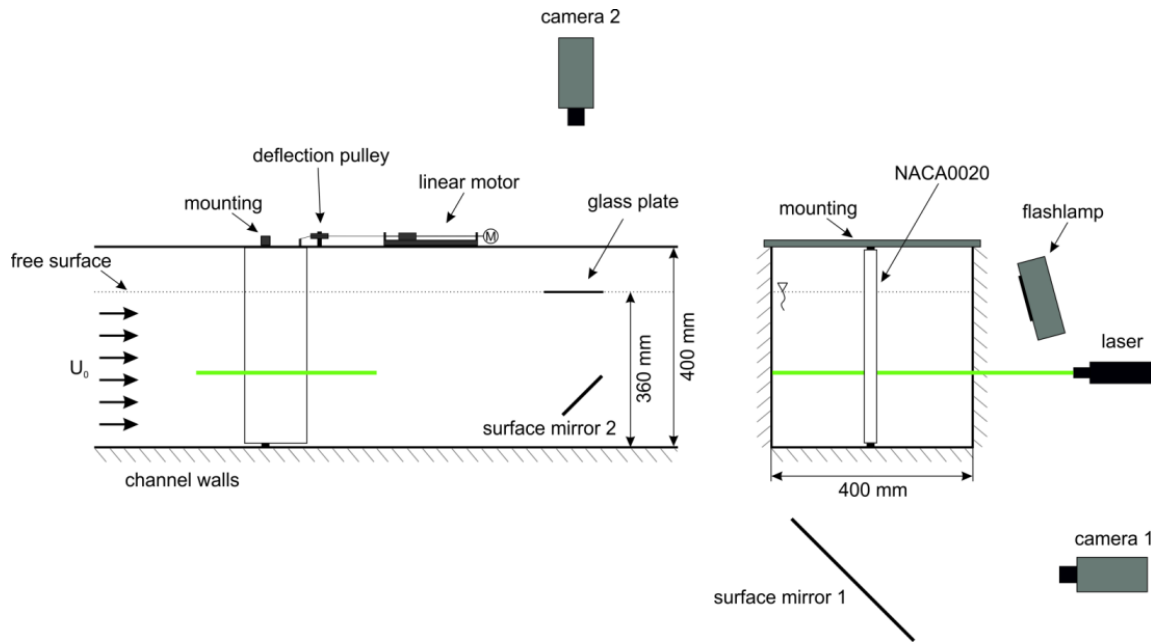

Figure 5: Diagram of the experimental setup for PIV measurements and simultaneous high-speed recordings of the flap motion around an airfoil in ramp-up motion.

3. Results

3.1. REFERENCE CASE AT STATIC STALL ANGLE OF ATTACK

Figure 6 presents the velocity contour plot for the plain airfoil (i.e. without hairy flaps) at $Re = 77 \times 10^3$ as a reference case for static stall angle of attack $\alpha_{ss} = 17.5°$. The flow field represents the average over 100 sample images. Positive values for streamwise velocity component U_x are depicted as solid lines; dashed lines represent negative velocities. One prominent feature that plays an important role in the stall process is the dynamics of the shear layer, which limit the recirculation region on the upper side of the airfoil as discussed in Mulleners & Raffel (2013). The chord-normal distance of this layer from the airfoil's upper surface yields a direct measurement of the size of the separation region, and is an appropriate value for the evaluation of stall process evolution and dynamics. In order to evaluate the chord-normal thickness of the separation region for each flap configuration, evaluation lines *E1* and *E2* were positioned perpendicular to the chord where the data yielded by the various experiments was compared. The first evaluation line (*E1*) was positioned near the leading edge ($x/c = 0.275$, $y/c = 0$), the second (*E2*) near the trailing edge ($x/c = 0.8$, $y/c = -0.2$). Parameter $\Delta\xi/c$

was defined as the chord-normal length of negative values of U_x. It indicates the average chord-normal width of the separation region equivalent to the mean distance of the shear layer from the wall (averaged along lines *E1* and *E2*).

Mulleners & Raffel (2013) used simultaneous PIV and force measurements to demonstrate that dynamic stall starts at the transition point where the primary instability stage with weak linear growth in $\Delta\xi/c$ (= $\Delta z/c$ in their experiment) progresses into a second state (known as the "vortex formation stage") accompanied by a steep increase in $\Delta\xi/c$. With the aid of simultaneous force measurements they consistently observed the onset of stall when the magnitude of $\Delta\xi/c$ reached a value of approximately 0.1 under various effective unsteadiness conditions. This provided a criterion for the definition of stall onset (i.e. when shear layer distance $\Delta\xi/c$ exceeds 0.1) on the basis of time-resolved PIV measurements despite the lack of direct lift-force measurements in the water channel. Note that this procedure closely adheres to the method proposed in Mulleners & Raffel (2013).
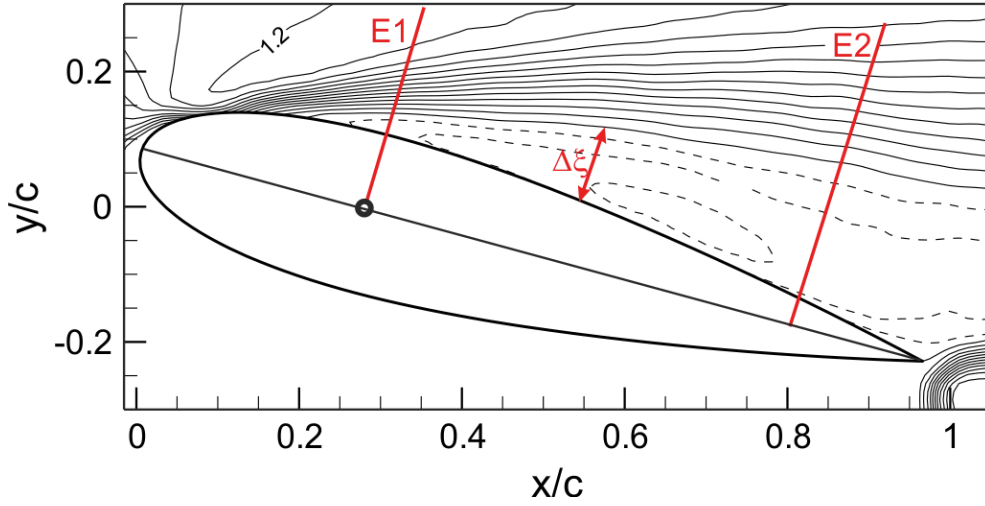
Figure 6: Contour lines of time-averaged stream-wise velocity component Ux normalized with free stream velocity U_∞ at Re = 77000 and static stall angle of attack α_{ss}= 17.5° for the clean airfoil without hairy flaps and the evaluation lines (*E1* and *E2*). Solid lines represent positive velocities, dashed lines negative velocities. Parameter $\Delta\xi/c$ is defined as the dimensionless chord-normal thickness of the separation region on the upper side of the airfoil.

A comparison between the airfoil without flaps and the modified airfoil is provided below in Figure 7. It is clearly demonstrated that the coating of hairy flaps significantly reduces the backflow region and prevents stall. Flow still remains attached at α=17.5° in the case of the airfoil covered with hairy flaps (configurations 4, 6). The latter configuration was the most effective of all configurations tested under static flow and angle of attack (see Table 1). Shorter flaps with a length of $L_F = 0.05c$ were not at all effective due to their insufficient reach into the separation region, thus dictating that near-wall flow was minimally affected by the presence of the flaps and separated all along the upper surface as

was observed in the case of the clean airfoil. On the other hand, long flaps with a length of $L_F = 0.2c$ as used in experiment no. 5 started to flutter because of their slenderness and flexural instability, thus delivering a somewhat chaotic motion pattern which was not clearly linked to flow dynamics. As a result, it was not possible to draw any conclusions about the fluid-structure interaction process from the flow studies. The sole focus of discussion in this paper is therefore the results yielded by flaps with a length of $L_F = 0.1c$ (no. 3, 4, 6 in Table 1). It is to be noted that these configurations also go into stall conditions at the larger angle of attack $\alpha_{ss}=20°$. This terminal angle of attack was therefore chosen for the ramp-up experiments in order to force the airfoil flow into full stall.
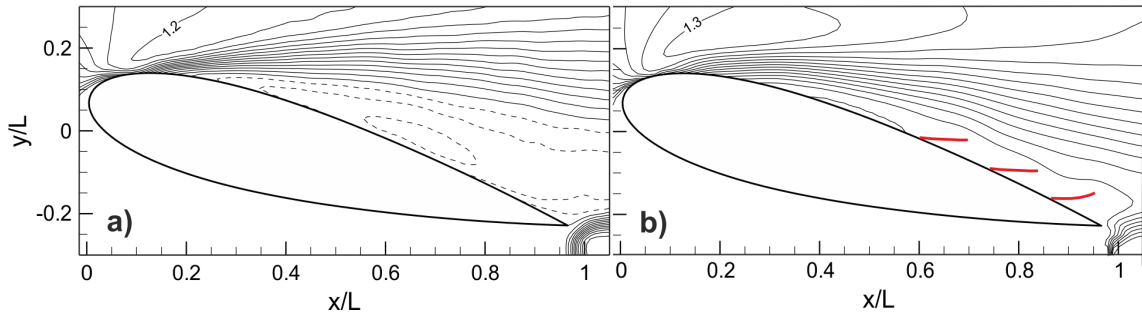

Figure 7: Comparison of mean flow properties of NACA0020 airfoil at angle of attack α=17.5° by means of contour lines for stream-wise velocity component Ux normalized with free stream velocity U_∞ at Re = 77×10³. a) Clean airfoil under stall conditions at $\Delta\xi/L \approx 0.12$. b) Airfoil covered with hairy flaps in configuration (triple row, no. 6) with fully attached flow and $\Delta\xi/L \approx 0$.

3.2.   RAMP-UP RESULTS

The magnitude of separation delay was estimated with the aid of the time resolved PIV-measurements. Time-span T_s (from the end of ramp-up motion to the time when $\Delta\xi/L$ exceeded 0.1) was therefore determined for the airfoils as described above. All measured values were normalized using time-span T_{sref} (reference case, same ramp-up motion). The results are presented in Table 1. The experiments were repeated several times, with final values only exhibiting marginal variations of less than 5%.

The results indicate that it is indeed possible to delay flow separation using dense rows of flexible flaps of this type, with the maximum delay observed in flap configuration no. 6 ($T_S/T_{sref} > 4$ when compared with the clean airfoil). In configuration no. 6 the flaps are positioned in three successive rows with an interspacing of $0.15c$ along the second half of the chord. The same interspacing is used in configuration no. 4, however the last row is skipped. In comparison with no. 6, the total effect of configuration no. 4 is smaller but still distinct ($T_S/T_{sref} = 2$). By way of contrast, double-rowed configuration no. 3 has larger interspacing ($0.3c$) and only exhibits a weak effect ($T_S/T_{sref} = 1.3$). This is a remarkable experimental outcome, as it shows that coatings with multiple individual slender flaplets are capable of delaying flow separation to a similar extent to that observed in the case of the long spanwise single flaps investigated in earlier

studies conducted by Schatz et al. (2004) or Johnston & Gopalarathnam (2012). As such, both interspacing between rows and the number of rows seem to play a role provided the individual flaps are of the same shape.

In view of the aforementioned results, high temporal resolution measurements were carried out for flap configuration no. 6 and the reference airfoil in order to investigate the specifics of the interaction between flap motion and the flow around the airfoil. A characteristic flap motion sequence is illustrated in Figure 8. The red arrow indicates three successive flaps in a streamwise direction (i.e. in the direction of the light-sheet).
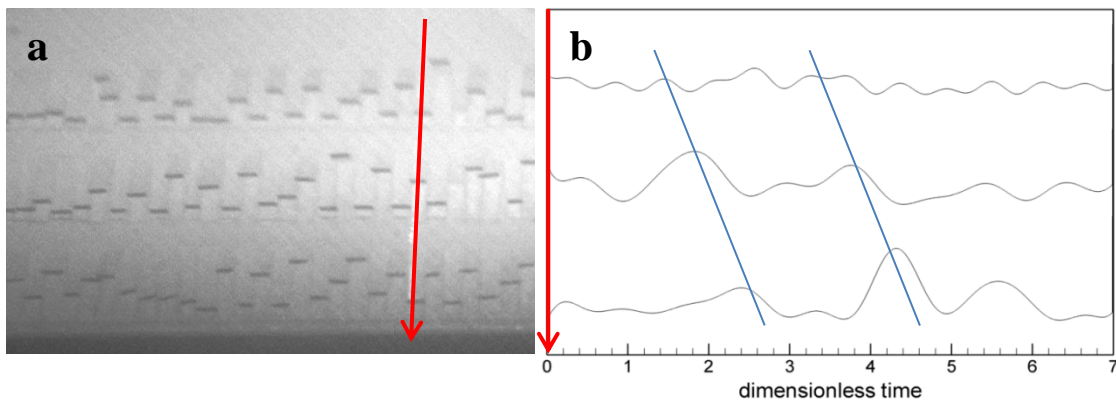

Figure 8: a) Instantaneous picture of the black-colored trailing edges of hairy flaps configured in three successive rows along the chord of the wing, as recorded by camera #2 from downstream. Note the zig-zag type variation in the elevation of the individual flaps along the array. b) Spatial-temporal reconstruction of the trailing edge, the vertical position of the hairy flaps is indicated along the red arrow as a function of dimensionless time t^* (time is made dimensionless using free stream velocity and chord length according to the following formula:

$t^* = t \cdot U_\infty/L$).Two significant events run in succession over the flaps at $t^* \approx 2$ and $t^* \approx 4$.

The events with significant elevation amplitudes shown in Figure 8 are signs of local flow structures moving over the flaps and inducing stronger changes in pressure distribution. In order to correlate flap motion events with flow features, additional information on vortex dynamics in the flow along the light-sheet position is provided in Figure 9. The Q-criterion was used to detect vortex cores in order to facilitate the identification of vortices within the 2D-PIV velocity fields.
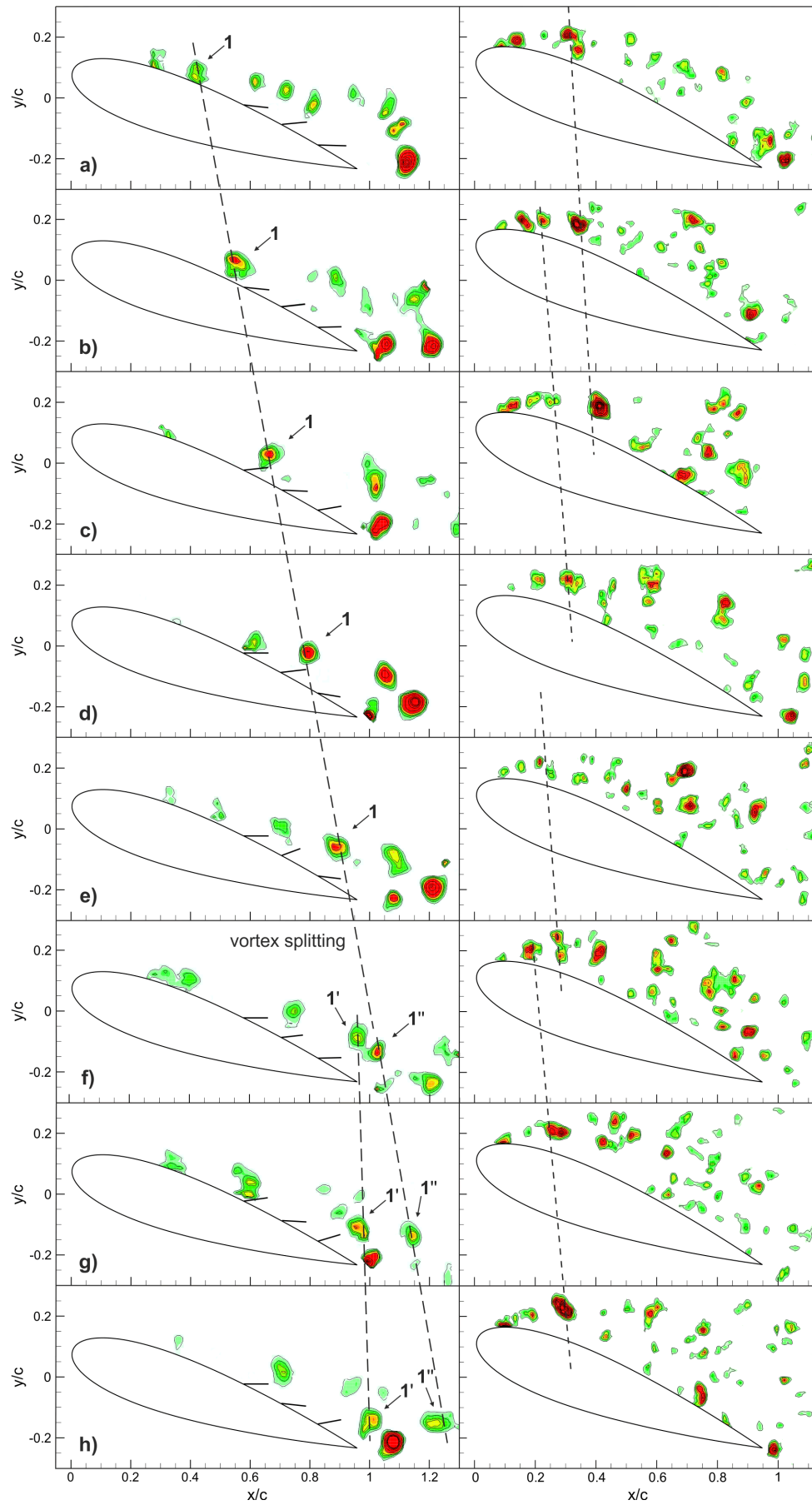
Figure 9: Vortex motion sequence (Δt^*=0.2) for flap configuration no. 6 (left) and reference airfoil (right) at Re = 77×10³ after ramp-up procedure. The images in the first row describe conditions at t^*=3.9 after ramp-up (see significant event in Figure 8).

The local maxima of positive Q represent roll-up vortices in the shear layer. This paper places special focus on the dynamics of these vortices in relation to recent studies conducted by Yarusevych et al. (2009) and Mulleners & Raffel (2013). Their results demonstrate that the non-linear process of the merging of roll-up vortices in the separated shear layer plays a key role in the transition from a slight increase in separation layer thickness $\Delta\xi/c$ to a steep increase and the onset of stall. This growth is linked to vortex pairing as a sub-harmonic component of fundamental disturbances. In light of this, Yarusevych et al. (2009) argue that the wavelength of fundamental disturbance λ_0 is the appropriate scale for a comparison between the roll-up process in boundary layer flows and in free shear layers. The alternative definition of the Strouhal number is therefore St* =$f_0\lambda_0/Ue$ where Ue denotes boundary-layer edge velocity. In this context, wavelength λ_0 can be expressed in terms of the propagation speed of roll-up vortices U_{drift} and roll-up frequency f_0 ($\lambda_0 =U_{\text{drift}}/f_0$), thus St* =$U_{\text{drift}}/U$e.

The sequence for the flap-covered airfoil shown on the left-hand side of Figure 9 illustrates the regular roll-up of the vortices in the shear layer, which forms rows

of vortices with relatively constant spacing along the chord of the wing. The typical wavelength of the fundamental disturbances is the spacing between the roll-up vortices measured for the lower half of the wing in Figure 9, or approx. λ_0 ≈ 0.15c-0.2c. In contrast, the reference airfoil exhibits more irregular vortices distribution. The formation of stronger vortices is already in evidence close to the leading edge. In configuration no. 6, the roll-up vortices are transported downstream without mutual interaction as indicated by the dashed lines. Their transportation velocity is $U_{drift} \cong 0.5\ U_\infty$, thus the Strouhal number is approx. Sr* = 0.45 ($U_e \approx 1.1\ U_\infty$). This falls well within the Strouhal number range of 0.45 < Sr* < 0.5 documented by Yarusevych et al. (2009) for the scaling of the fundamental frequency with the wavelength of fundamental disturbances in the shear layer above an airfoil at various angles of attack (0°-10°).

In case of the clean airfoil, the roll-up vortices already interact with one another at an early stage in the roll-up process. Images a-c in Figure 9 show vortex pair interaction at streamwise location x/L≈0.3. The consequence of that vortex pair interaction is the overtaking of the leading vortex by the trailing vortex in a type of roller motion with final merging. As a result, strong wall-normal motion is induced and lifts the vortex off the wall. The region of flow deceleration therefore grows in wall-normal direction. As a consequence, the convection velocity of the pair is locally reduced, as is evident in the steeper slope of the lines ($U_{drift} \cong 0.2\ U_e$). In contrast, the type of shear-layer vortex interaction

22

observed in the case of configuration no. 6 is not in evidence in the results for the clean airfoil. Several other events similar to one described above in combination with the clean airfoil are indicated by the dashed lines in Figure 9. It is clear that the vortex pairing represents the sub-harmonic peak observed by Yarusevych et al. (2009) in a separated shear layer. Here again, this type of process is linked to the onset of stall as documented in Mulleners & Raffel (2013). It appears that a wing with flaplets on its surface keeps the shear-layer in its linear stage for a longer period than a clean airfoil. It is to be noted that double-row configuration no. 4 exhibits similar interspacing between rows to no. 6 and is also characterized by a considerable delay in Ts (a factor of around 2), whereas the larger interspacing of case 5 only exerts a minor influence. The observations made in this paper show that interspacing between rows in configurations characterized by considerable stall delay (4, 6) is in the order of the fundamental wavelength of the shear layer. This points towards possible mode locking with structures that may delay or even prevent the non-linear growth process which includes vortex merging.

Another striking observation is the change in characteristic flap motion frequencies along the chord. Figure 8 shows that the first row of flaps is excited at a relatively regular frequency which corresponds with fundamental frequency f_0 of the shear-layer vortices in this region ($f_0 \approx 2$-$2.5\ U_\infty/c$). Further downstream, the flap motion amplitude increases as frequency decreases. This indicates more

significant interaction between the vortices and the flaps in the 2nd and 3rd row, which is documented on the left-hand side of Figure 9 in the form of a dashed line along the path of a larger vortex. Vortex #1 is initially formed in the shear layer at *x/c*=0.4 and subsequently transported downstream at nearly constant velocity ($U_{drift} \cong 0.5\ U_0$). After passing the 2nd row, it starts to split up into two parts as a consequence of interaction with the flap in the last row. The movement of vortex #1´´ further downstream remains unaffected, while vortex section #1´ ceases its motion and remains near the flap edge. The splitting process is accompanied by the growth of a starting vortex at the trailing edge of the wing which in itself indicates a temporal increase in bound circulation around the wing. This starting vortex is then shed into the wake as depicted in Figure 10.

4.   Conclusions

The present study is a continuation of our work on fluid-structure interaction in structures covered with flexible flaplets (see Kunze and Brücker 2011), and has been adapted to the application of passive separation control in airfoils. In comparison with earlier studies on this subject (see, for example, Bramesfeld and Maughmer (2002), Schatz et al. (2004) and Yarusevych et al. (2009)), the effector structures used take the form of dense rows of slender, flexible flaplets that respond individually to the flow and only interact with the flow to a limited

extent due to their relatively low non-dimensional bending stiffness of $K=O(10^{-2}$-$10^{-4})$. A detailed investigation into interaction between the flaps and the flow field was carried out by taking simultaneous recordings of flap motion and flow field using two high-speed cameras. This made it possible to study the correlation between the vortex roll-up process in the developing shear layer and the interaction between the vortices and the flaps.
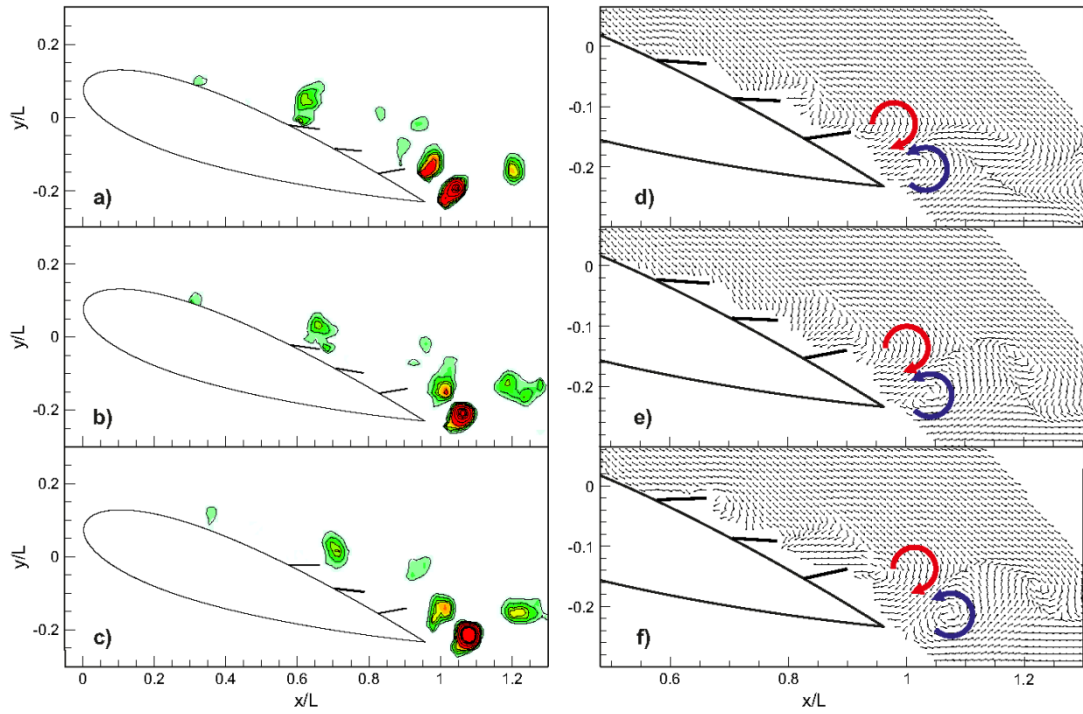

Figure 10: Illustration of vortex-pair interaction at the trailing edge of the airfoil for flap configuration no. 6. A sequence ($\Delta t^*=0.06$) of vortex motion (Q-criterion on the left) and the corresponding velocity-vector field (a streamwise velocity of 40% of free stream velocity U_∞ has been subtracted) is depicted. The first-row images show the situation at $t^*=5.25$ sec after the ramp-up procedure.

Special emphasis is devoted here to the analysis of not only a ramp-up procedure which forces the flow to go into stall, but also the way in which the presence of flaplets modifies this process in comparison with a clean airfoil. As the stall process is qualitatively similar in the case of airfoils subjected to either oscillating or ramp-type motions (McCroskey 1981), the latter motion type was chosen for reasons of improved synchronization between the measurement technique and airfoil motion. High-speed PIV measurements enabled the determination of the evolution of chord-normal thickness $\Delta\xi/c$ in the separation region as an indicator of stall onset. Stall onset starts when the weak linear growth stage gives way to non-linear rapid growth accompanied by vortex merging. According to the work of Mulleners & Raffel (2013) in the field of dynamic stall at similar reduced frequencies to those dealt with in this paper, the onset of stall which corresponds with the measured drop in lift force occurs when $\Delta\xi/c$ reaches a critical value of $\Delta\xi/c\approx0.1$. This has been verified using simultaneous flow and lift force measurements. Using this critical value to determine stall onset time Ts, it was possible to demonstrate that in some configurations the slender flaps are indeed able to delay stall by a factor of around 2-4 when compared with a clean airfoil. All configurations took the form of dense rows of flaplets on the lower half of the wing in a chord-wise range of $0.58c - 0.98c$, with previous studies having shown this location to be where effectors are at their most active. The configurations that exhibited a considerable

effect (4, 6) featured flaplets with a length of L=0.1c aligned in double or triple rows with chord-wise interspacing of 0.15c-0.2$\underline{c}$. Smaller flaplets with a length of L=0.05c were not at all effective, and this was attributed to the small chord-normal distance over which they can deploy, which dictates that they do not reach sufficiently deep into the boundary layer region. On the other hand, longer flaplets with a length of L=0.2c were not practical as a result of their weak flexural stability, which led to a somewhat chaotic flutter motion that prohibited any conclusions regarding the flow interaction process.

The major difference between the flap-covered airfoil and the clean airfoil in terms of flow evolution along the upper surface of the airfoil is the more regular roll-up of shear-layer vortices observed in the former, with the latter characterized by the early development of complex vortex interactions in the form of vortex pairing that leads to a rapid non-linear transition into stall (also see Mulleners & Raffel (2013)). This suggests that the flaplets interact with the dynamics of the stall process in a way that delays transition into the non-linear stage. If the measured drift velocity of the vortices U_{drift} and their characteristic wavelength λ_0 are compared with measurements gathered for airfoils at similar Reynolds numbers in a non-dimensional form of the Strouhal number Sr* indicated in Yarusevych et al. (2009), the result of Sr*≈0.45 arrived at in this paper falls well within the range $0.45 \leq$ Sr* ≤ 0.5 which represents the linear stage of growth in fundamental disturbance in the shear layer. This gives a clear

indication that the regular arrangement of the vortices is the result of the roll-up of the shear layer in the fundamental instability mode.

When the vortices are transported across the rows of the flaps, the excitation of the flaps moves downstream in a wave-like motion with an increasing amplitude of flap elevation in streamwise direction. The leading row exhibits the typical frequency of the fundamental instability as the vortices pass by. As configurations no. 4 and 6 are characterized by roughly the same row interspacing of $\Delta x/c$=0.15-0.2 and both have a considerable delaying effect on stall onset, it is concluded that interspacing plays an important role in the observed process. Their interspacing is actually similar to the measured characteristic wavelength of the roll-up vortices λ_0, and it is therefore concluded that the flap rows trigger mode locking in the roll-up process. This may explain the weak impact of the effectors when interspacing or flap length is too large. It is to be noted that a cross-check of these results against those for an airfoil equipped with double-rows of non-flexible flaps at a fixed angle of 30° (the mean angle of deployed flaps in the first row) and an interspacing of 0.15c yielded stall delay results at Ts/Tsref≈1.8 which were similar to those arrived at for configuration no. 4. The effect observed therefore does not seem to be linked to the motion of the flaps, but instead to the specific chord-wise arrangement thereof in relation to the fundamental wavelength. In practice, flexible flaps

should nevertheless be preferred to fixed flaps due to the minimization of parasitic drag ensured by their self-adaptive motion.

Strong fluid-structure interaction is in evidence in the most downstream row of flaplets close to the trailing edge. Vortex splitting occurs, with some vorticity captured and accumulated on the lee side of the flaps. This is counterbalanced by the growth of a starting vortex at the trailing edge of the wing. According to the principles of the Kutta condition, this is accompanied by a simultaneous increase in bound circulation. Both vortices are then shed together into the wake as a pair.

It should not go unmentioned that the observed process was only tested at a low Reynolds number flow $Re=77\times10^3$ along an NACA0020 airfoil at a reduced frequency of $k=0.12$ in combination with a specific configuration of flexible flaps (bending stiffness, material). The fundamental frequency of the roll-up process is expected to scale with the Reynolds number and the angle of attack detailed in Yarusevych et al. (2009). As such, mode locking requires the flaps to be arranged in a specific way which changes according to those parameters. Additional testing involving the variation of both the materials used and the interspacing relative to the fundamental instability of the flow needs to be conducted in order to support a more general conclusion about the usefulness of flexible flaplets as passive flow control devices. Their outstanding feature is that they can be applied simply by coating the surface. In addition, the fact that each flaplet has only a

small span and reacts individually to the flow means that the reactive forces on the airfoil may average up in a smoother way due to the temporal variations in flap action along the span.

Acknowledgements

References

Bechert, D.W., Bruse, M., Hage, W., Meyer, R., 1997. Biological surfaces and their technological application — laboratory and flight experiments on drag reduction and separation control. AIAA Paper 97-1960.

Bramesfeld, G., Maughmer, M. D., 2002. Experimental investigation of self-actuating, upper-surface, high-lift-enhancing effectors. Journal of Aircraft 39, 120-4.

Brücker, Ch., 2011. Interaction of near-wall turbulence with flexible hairs. Journal of Physics: Condensed Matter 23, 18-29.

Carruthers, A. C,, Thomas, A. L. R., Taylor. G. K., 2007. Automatic aeroelastic devices in the wings of a steppe eagle Aquila nipalensis. Journal of Experimental Biology 210, 4136-49.

Favier, J., Dauptain, A., Basso, D., Bottaro, A., 2009. Passive separation control using a self-adaptive hairy coating. Journal of Fluid Mechanics 627, 451-483.

Hu, H., Tamai, M., Murphy, J.T., 2008. Flexible membrane airfoils at low Reynolds numbers. Journal of Aircraft 45(5), 1767–1778.

Johnston, J. and Gopalarathnam, A., 2012. Investigation of a bio-inspired lift-enhancing effector on a 2D airfoil," Bioinspiration & Biomimetics, Vol. 7, No. 3, 2012, Bioinspir. Biomim. 7 036003. DOI:10.1088/1748-3182/7/3/036003

Kunze, S., Brücker, Ch., 2012. Control of vortex shedding on a circular cylinder using self-adaptive hairy flaps. Comptes Rendus Mécanique 340(1-2), 41-56.

Liebe, A., 1979. Der Auftrieb am Tragflügel: Entstehung und Zusammenbruch. Aerokurier 12, 1520.

McCroskey, W. J., 1981. The phenomenon of dynamic stall. Tech. rep. NASA

Mulleners, K., Raffel, M., 2012. The onset of dynamic stall revisited. Experiments in Fluids 52(3), 779-793.

Mulleners, K.; Raffel, M,, 2013. Dynamic stall development. Experiments in Fluids 54:1469, DOI 10.1007/s00348-013-1469-7

Ponitz B, Schmitz A, Fischer D, Bleckmann H, Brücker C (2014) Diving-Flight Aerodynamics of a Peregrine Falcon (Falco peregrinus). PLoS ONE 9(1): e86506. doi:10.1371/journal.pone.0086506

Schatz, M., Knack. T., Thiele, F., Mey, R., Hage, W., Bechert, D.W., 2004. Separation control by self-activated movable flaps. AIAA paper 2004-1243.

Tang, D., Dowell, E.H., 2007. Aerodynamic loading for an airfoil with an oscillating gurney flap. Journal ofAircraft 44(4), 1245 – 1257.

Schlüter, J. U., 2009. Lift Enhancement at low Reynolds numbers using pop-up feathers. AIAA Paper 2009-4195.

Venkataraman, D., Bottaro, A., 2012. Numerical modeling of flow control on a symmetric aerofoil via a porous, compliant coating. Physics of Fluids 24(9)

Yarusevych S, Sullivan P.E., Kawall J.G., 2009. On vortex shedding from an airfoil in low-Reynolds number flows. Journal of Fluid Mechanics 632, 245-271.

Figure Captions

Figure 1. A falcon with popped-up feathers (left: frontal view, right: side view) during gliding flight before landing (from the measurement campaign documented in Ponitz et al. 2014).

Figure 2: Dimensions of the NACA0020 airfoil and parameters of the hairy flap configuration

Figure 3: NACA0020 airfoil with flexible hairy flaps (configuration No. 6).

Figure 4: Image of the field of view for a hairy flap configuration (No. 6) at constant angle of attack α=17.5°.

Figure 5: Diagram of the experimental setup for PIV measurements and simultaneous high-speed recordings of the flap motion around an airfoil in ramp-up motion.

Figure 6: Contour lines of the time-averaged stream-wise velocity component Ux normalized with free stream velocity U_∞ at Re = 77×10^3 and a constant angle of attack α=17.5° for the NACA0020 airfoil without hairy flaps and the evaluation lines ($E1$ and $E2$). Solid lines represent positive velocities, dashed lines negative velocities. Parameter $\Delta\xi/c$ is defined as the average thickness of the separation bubble.

Figure 7: Comparison of mean flow properties of NACA0020 airfoil at α=17.5° angle of attack by means of contour lines for stream-wise velocity component Ux normalized with free stream velocity U_∞ at Re = 77×10^3. a) Plain airfoil, b) airfoil covered with hairy flaps (configuration No. 6).

Figure 8: a) Instantaneous picture of the black-colored trailing edges of hairy flaps configured in three successive rows along the chord of the wing, as recorded by camera #2 from downstream. Note the strong zig-zag type variation in the elevation of the individual flaps along the array. b) Spatial-temporal reconstruction of trailing edge, the vertical position of the hairy flaps is indicated along the red arrow as a function of dimensionless time t^* (time is made dimensionless using free stream velocity and chord length according to the following formula: $t^* = t \cdot U_\infty / L$). Significant events occur at $t^* \approx 2$ and $t^* \approx 4$ at the downstream row.

Figure 9: Vortex motion sequence ($\Delta t^* = 0.2$) for flap configuration no. 6 (left) and clean reference airfoil (right) at $Re = 77 \times 10^3$ after ramp-up procedure. The pictures in the first row represent the situation at $t^* = 3.9$ after ramp-up (compare with significant event in Figure 8).

Figure 10: Illustration of vortex-pair interaction at the trailing edge of the airfoil for the flap configuration no. 6. A sequence ($\Delta t^* = 0.06$) of vortex motion (Q-criterion left) and the corresponding velocity-vector-field (a streamwise velocity of 40% of free stream velocity U_∞ has been subtracted) is depicted. The first-row images show the situation at $t^* = 5.25$ sec after the ramp-up procedure.

34